Supporting Information

Tailoring Isolated Cu−N_4 and Fe−N_4 Atomic Sites for Efficient Selective Electroreduction of CO_2 to CO

Saixi Chen[1#], Ning Li[2#], Hongxiang Li[1], Jinglei Wu[1], Aoshen Liu[1], Xinchen Zhang[1], Yan Su[2], Kun Zhao[1]*

[1] College of Environmental Science and Engineering, North China Electric Power University, Beijing 102206, China.

[2] Key Laboratory of Materials Modification by Laser, Ion and Electron Beams (Dalian University of Technology), Ministry of Education, Dalian 116024, China

*Email: zhao.k@ncepu.edu.cn (K. Zhao)

Experimental section

Chemicals and Materials

All chemicals were of analytical grade and used as received. The reagents used were potassium bicarbonate ($KHCO_3$, ≥99.5%), 2-methylimidazole (99%), zinc acetate dihydrate ($Zn(OAc)_2·2H_2O$, 98%), anhydrous copper (II) acetate ($Cu(OAc)_2$, 99%), iron(II) acetate ($Fe(OAc)_2$, 95%), iron phthalocyanine (FePc, 97%), copper phthalocyanine (CuPc, 98%), KCl (99.8%), KBr (99.5%), potassium dihydrogen phosphate (KH_2PO_4, ≥99%), and dipotassium hydrogen phosphate (K_2HPO_4, ≥99%). Nafion-related materials comprised Nafion solution (5 wt%) and Nafion 117 membranes. Gases: CO_2 (99.999%) and Ar (99.999%). Deionized water (18.2 MΩ·cm at 25 °C) was used for all solution preparations and equipment rinses.

Synthesis of Catalysts

In synthesizing the catalyst Cu-FeSA, a mixed solution A was first prepared by dissolving 5.96 g zinc acetate dihydrate ($Zn(OAc)_2·2H_2O$) and 1.24 g anhydrous copper acetate ($Cu(OAc)_2$) in 120 mL deionized water. Separately, 22.33 g 2-methylimidazole was dissolved in 120 mL deionized water to form solution B. Solutions A and B were combined under vigorous stirring at 25 °C for 1 h, followed by static aging for 4 h. The resulting off-white precipitate was collected via vacuum filtration, washed with deionized water, and dried at 60 °C to obtain the precursor. The Cu-FeSA catalyst was synthesized by homogenizing 0.4 g of ZIF-8 precursor, 0.02 g FePc, 0.2 g KCl, and 0.6 g KBr through mortar grinding, followed by pyrolysis at 950 °C for 4 h under N_2 atmosphere (5 °C min^{-1} heating rate). The resulting black powder was washed with deionized water and vacuum-dried. The CuSA and FeSA was synthesized except for adding 1.24 g of anhydrous copper acetate or 1.19 g of iron acetate into the solution A.

DFT calculations

Density functional theory calculations for all materials were performed with the Vienna ab initio Simulation Package (VASP).[1,2] The Perdew–Burke–Ernzerhof (PBE) exchange-correlation functional was adopted.[3] The Kohn–Sham wave functions were expanded in a plane-wave basis set with an energy cutoff of 500 eV, and the core–valence interactions were described by projector augmented-wave (PAW) pseudopotentials.[4] Geometry optimizations were carried out until convergence thresholds of 10^{-5} eV in total energy and 10^{-2} eV/Å in atomic forces were reached. For 2D slab models, a vacuum spacing of no less than 15 Å was applied perpendicular to the layer to suppress artificial coupling between periodic replicas. The Brillouin zone sampling for these systems employed a 2×2×1 Monkhorst–Pack k-point grid. Notably, the calculation of Gibbs free energy includes zero-point energy (ZPE).

The adsorption energy (E_{ad}) of the structures was calculated using the equation:

$$E_{ad} = E_{surface + adsorbate} - E_{surface} - E_{adsorbate} \quad (1)$$

where $E_{surface + adsorbate}$, $E_{surface}$ and $E_{adsorbate}$ represent the total electronic energy of the adsorption system, the individual surface, and the adsorbate, respectively.

Furthermore, the free energy change (ΔG) is defined by:

$$\Delta G = \Delta H - T\Delta S \quad (2)$$

where ΔH and ΔS represent the variation of enthalpy and entropy respectively.

CO_2RR Performance Test

The electrochemical measurements were conducted in a three-electrode system using a CHI760E workstation at 25°C. Catalyst ink—prepared by homogenizing 10 mg catalyst with 0.3 mL Nafion solution (5 wt.%) in 2.7 mL deionized water—was uniformly coated onto HCP331P carbon cloth (3.6 × 2.7 cm^2) as the cathode (loading: 1.03 mg cm^{-2}). A saturated KCl Hg/Hg_2Cl_2 electrode served as the reference electrode with a Pt sheet counter electrode. CO_2 was continuously purged into the cathode chamber at 100 mL min^{-1}.

CO_2RR Product Analysis

The gaseous products were analyzed using a Shimadzu GC-2014 gas chromatograph equipped with an RT-Q-Bond capillary column. The liquid products were characterized using ion chromatography (Metrohm ECO IC). The Faradaic efficiencie (FE) were calculated as:

$$FE = C \times V \times Z \times F/Q \times 100\% \quad (3)$$

where C = product concentration, V = total reaction volume, Z = electron transfer number, F = Faraday constant (96,485 C mol^{-1}), and Q = total charge passed during electrolysis.

Supplementary Figures

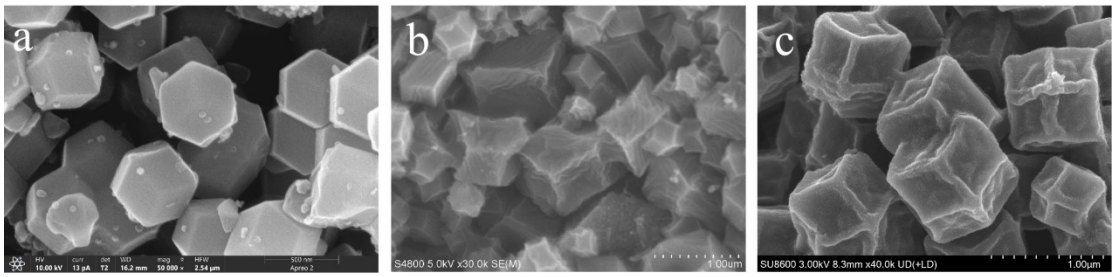

Figure S1. SEM image of CuSA, FeSA, Cu-FeSA revealed their rhombic dodecahedron morphology.

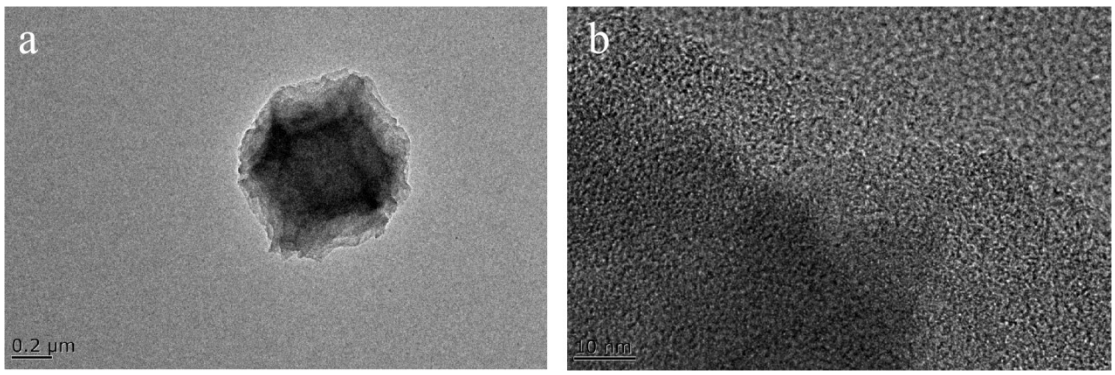

Figure S2. TEM image of Cu-FeSA indicated the metal-free particles in the catalyst.

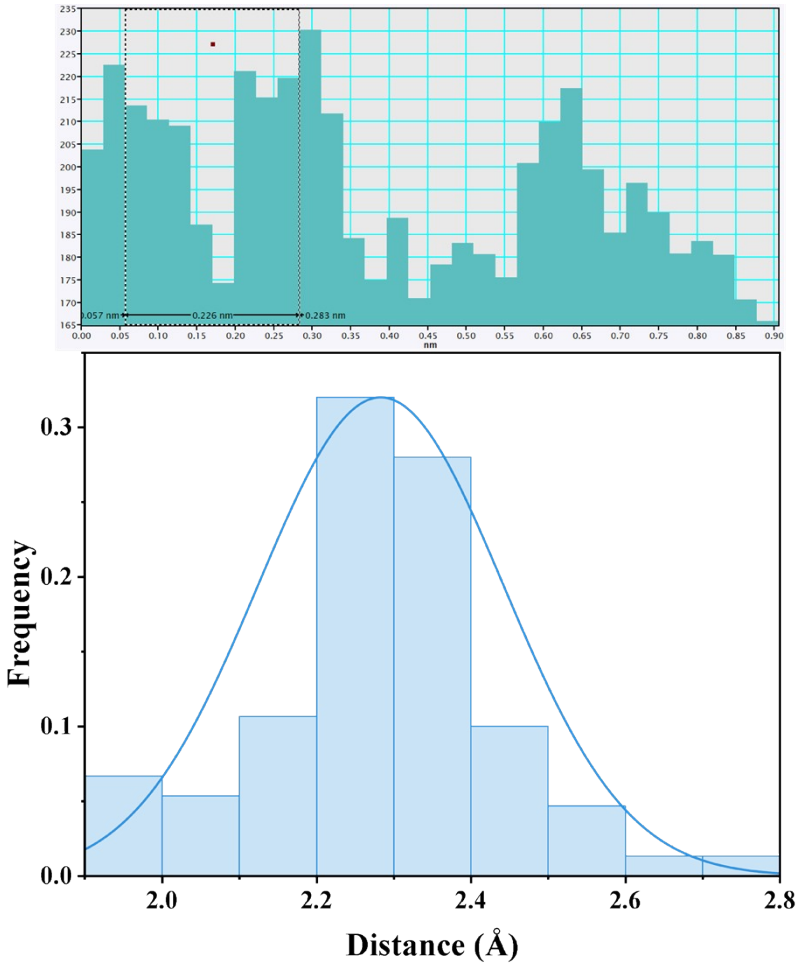

Figure S3. Distance distribution diagram of Cu single atom and Fe single atom.

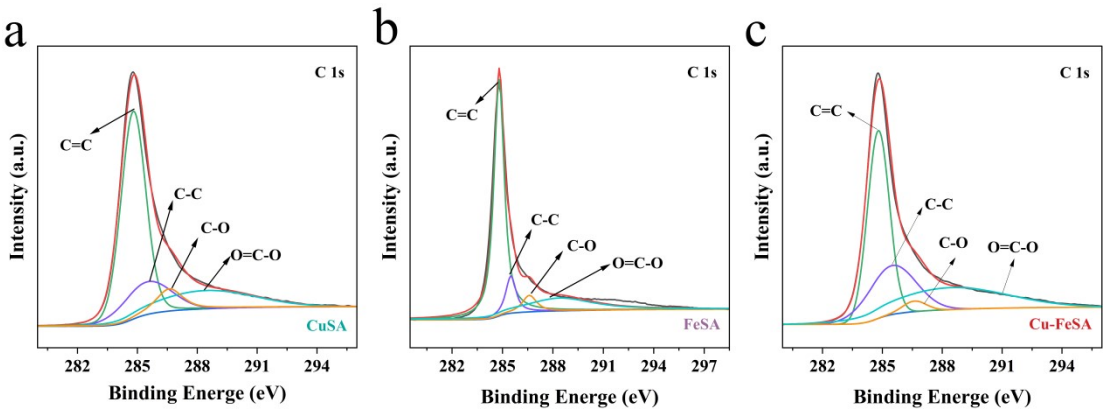

Figure S4. High-resolution XPS spectra of C 1s for CuSA, FeSA and Cu-FeSA.

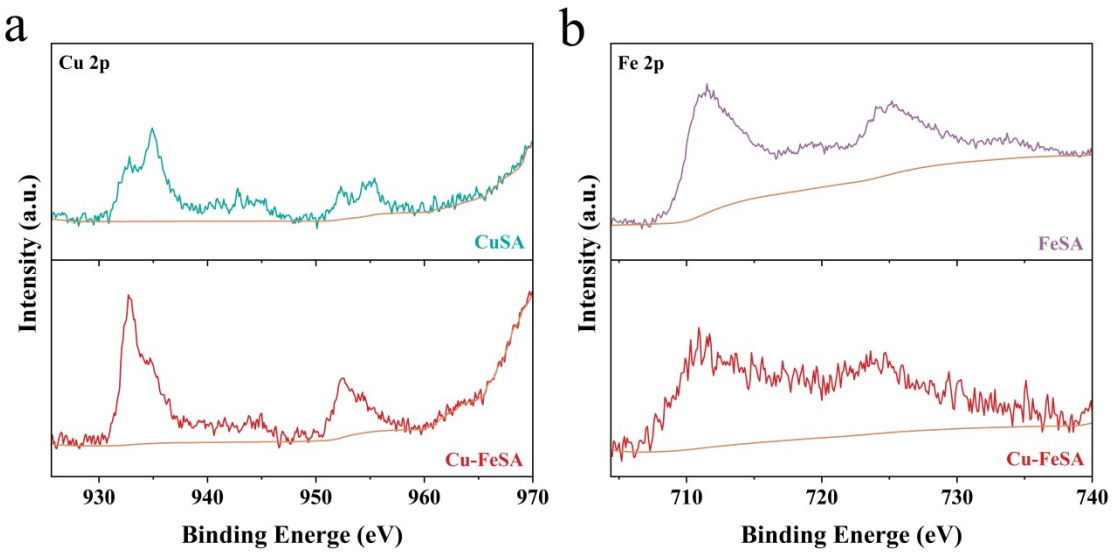

Figure S5. (a) High-resolution XPS spectra of Cu 2p for CuSA and Cu-FeSA, (b) High-resolution XPS spectra of Cu 2p for FeSA and Cu-FeSA.

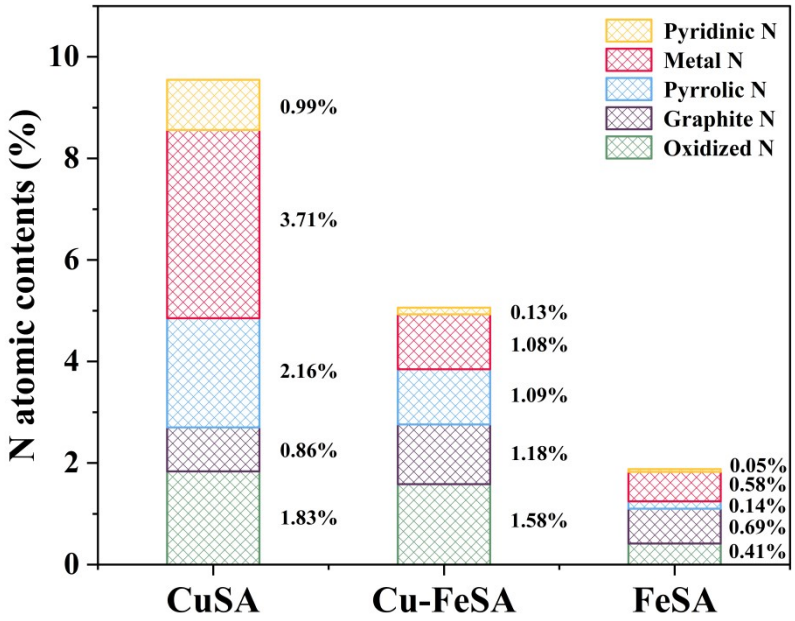

Figure S6. Various N types of catalysts in different monatomic forms obtained by XPS statistics.

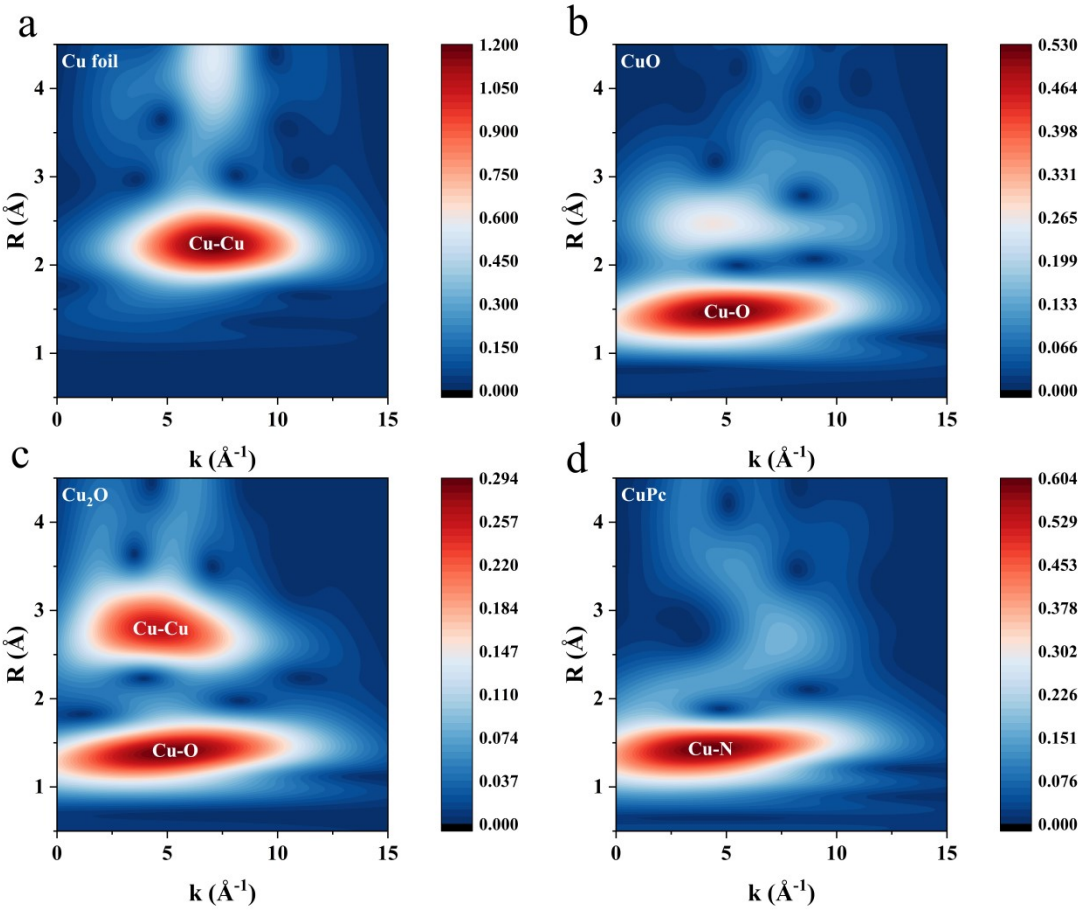

Figure S7. The wavelet transform of the Cu foil, CuO, Cu_2O and CuPc.

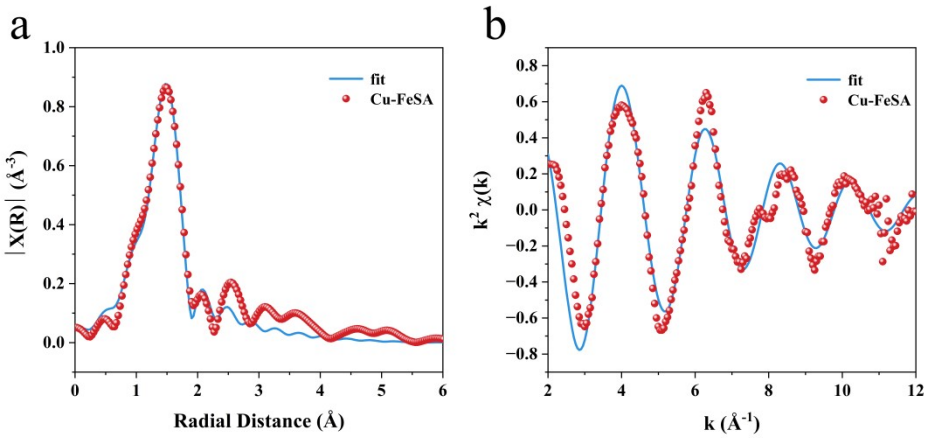

Figure S8. (a) Cu K-edge EXAFS and fit for the Cu-FeSA, shown in k^2 weighted R-space. (b) Cu K-edge EXAFS and fit for the sample, shown in k^2 weighted k-space.

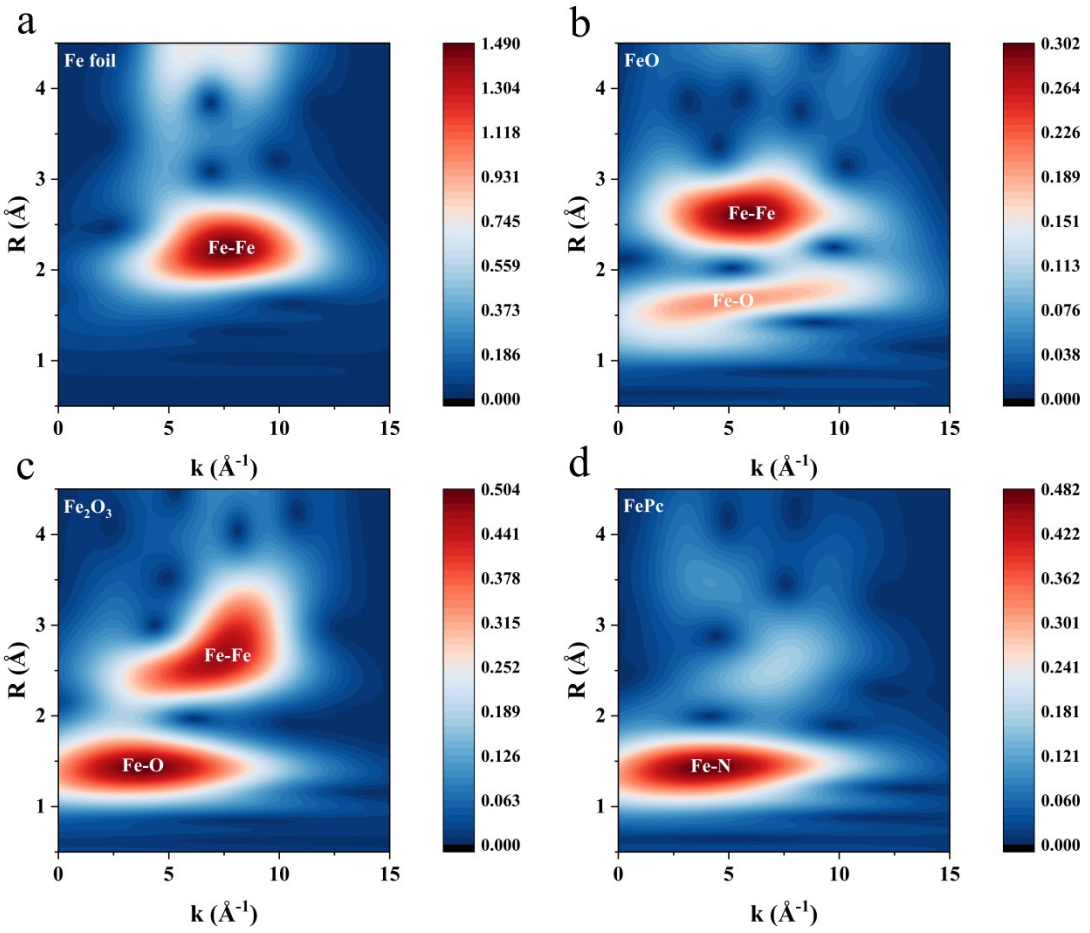

Figure S9. The wavelet transform of the Fe foil, FeO, Fe_2O_3 and FePc.

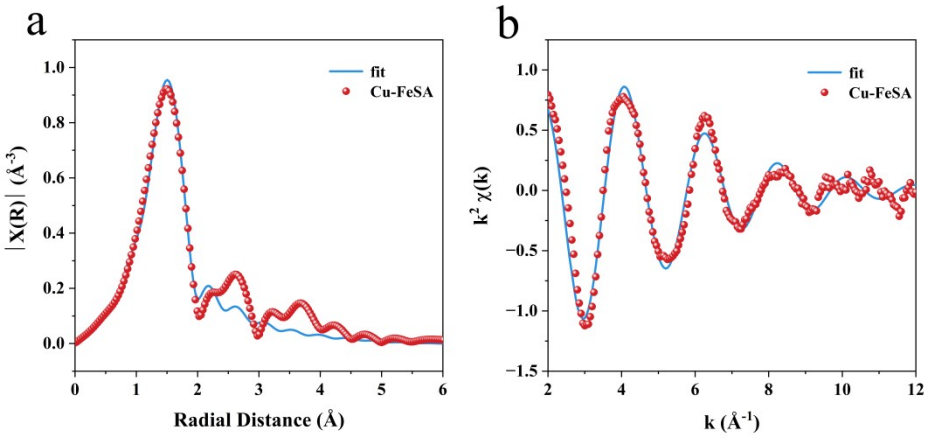

Figure S10. (a) Fe K-edge EXAFS and fit for the Cu-FeSA, shown in k^2 weighted R-space. (b) Fe K-edge EXAFS and fit for the sample, shown in k^2 weighted k-space.

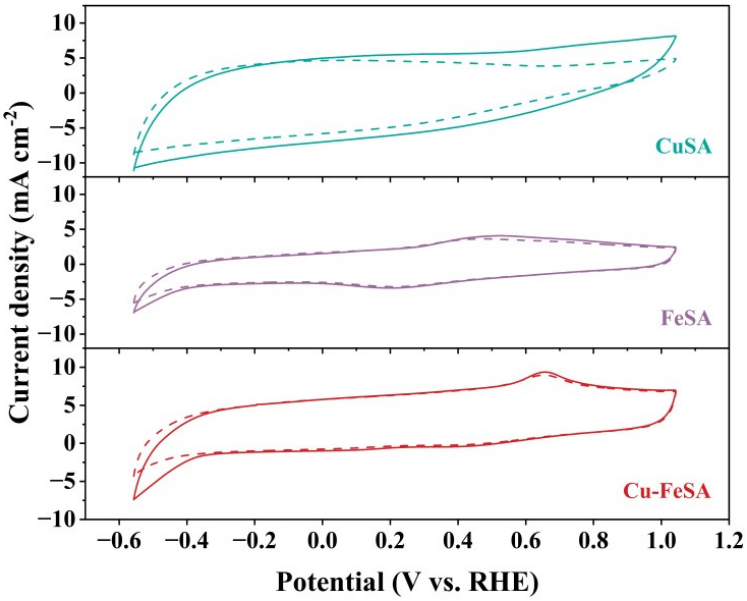

Figure S11. CV curves of CuSA, FeSA and Cu-FeSA.

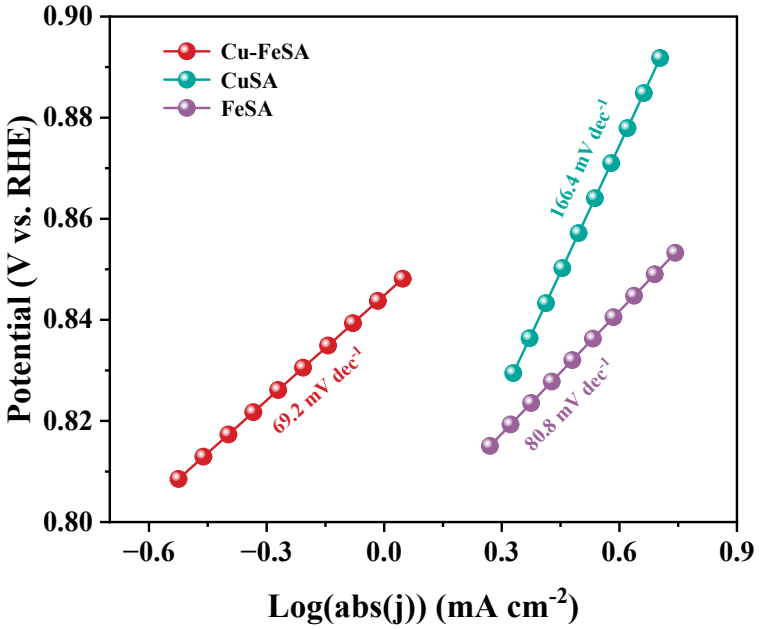

Figure S12. Tafel slope of Cu-FeSA, CuSA and FeSA.

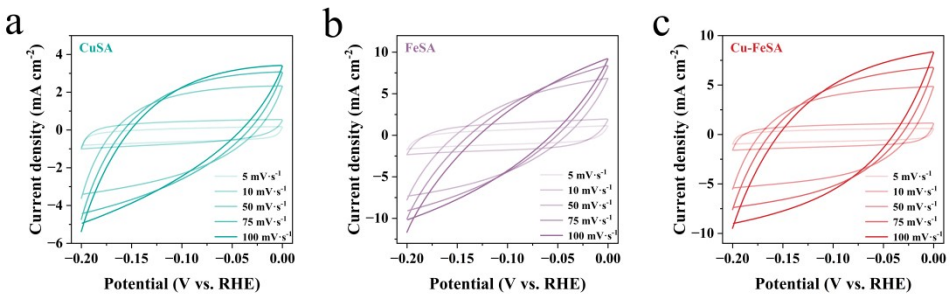

Figure S13. Cyclic voltammetric curves of CuSA, FeSA and Cu-FeSA at different scan rates from 5 mV s^{-1} to 100 mV s^{-1}.

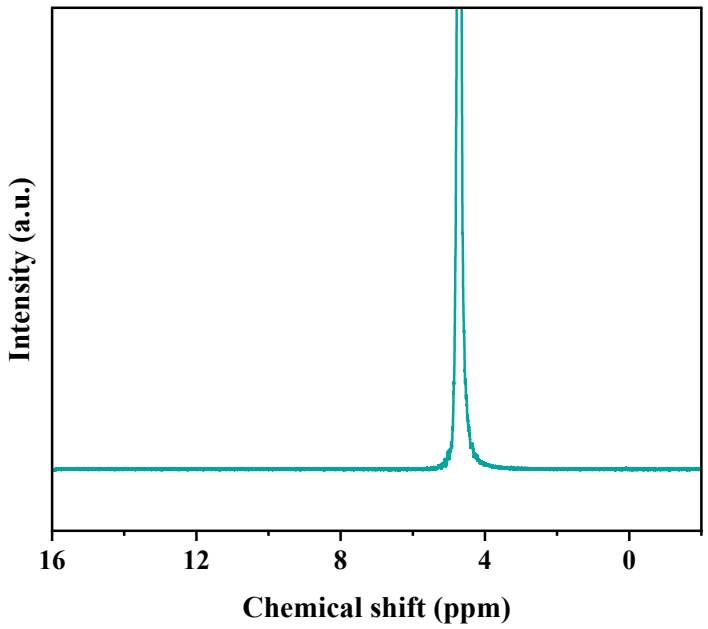

Figure S14. The detection of liquid products on Cu-FeSA by ^{1}H NMR at −1.26 V.

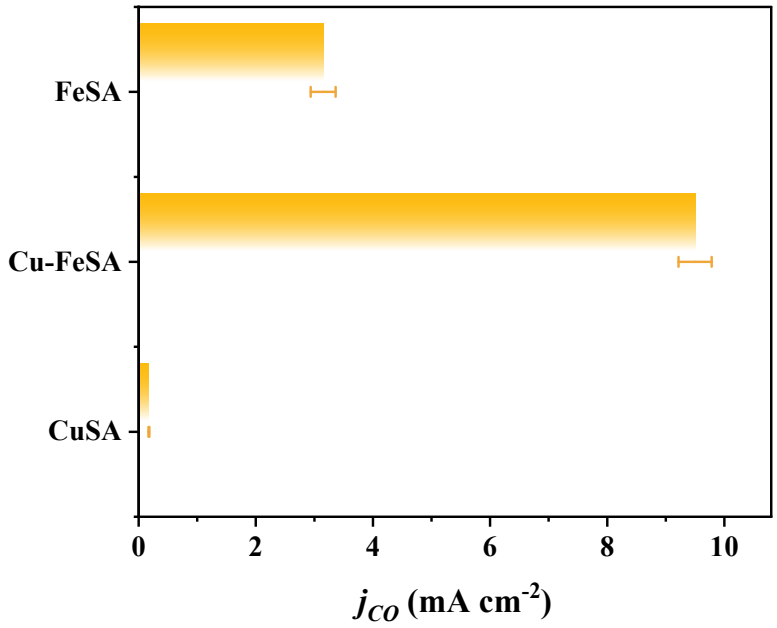

Figure S15. CO partial current density for CuSA, FeSA and Cu-FeSA at −1.26 V (vs RHE).

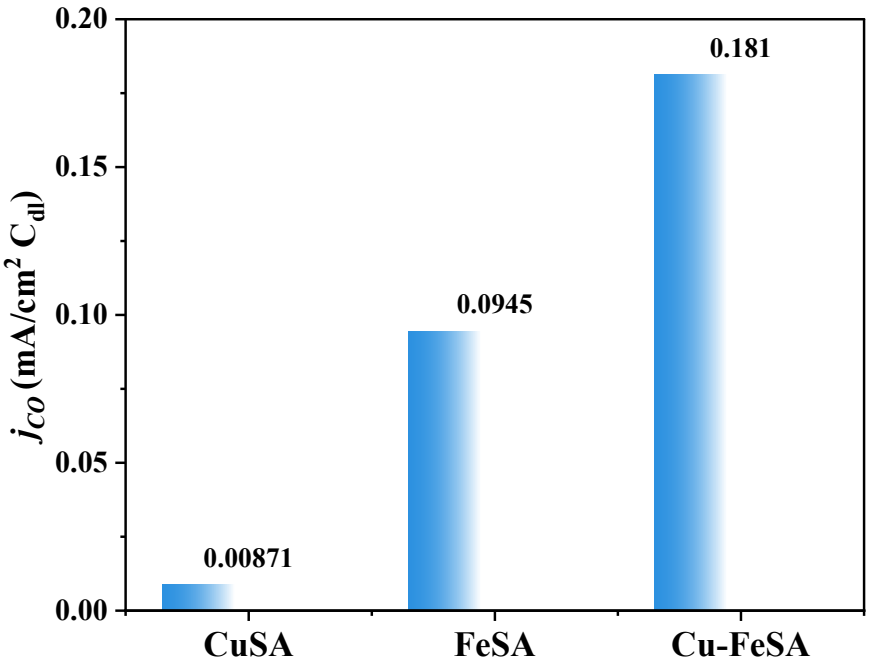

Figure S16. ECSA-normalized CO partial current densities for CuSA, FeSA and Cu-FeSA at −1.26 V (vs RHE).

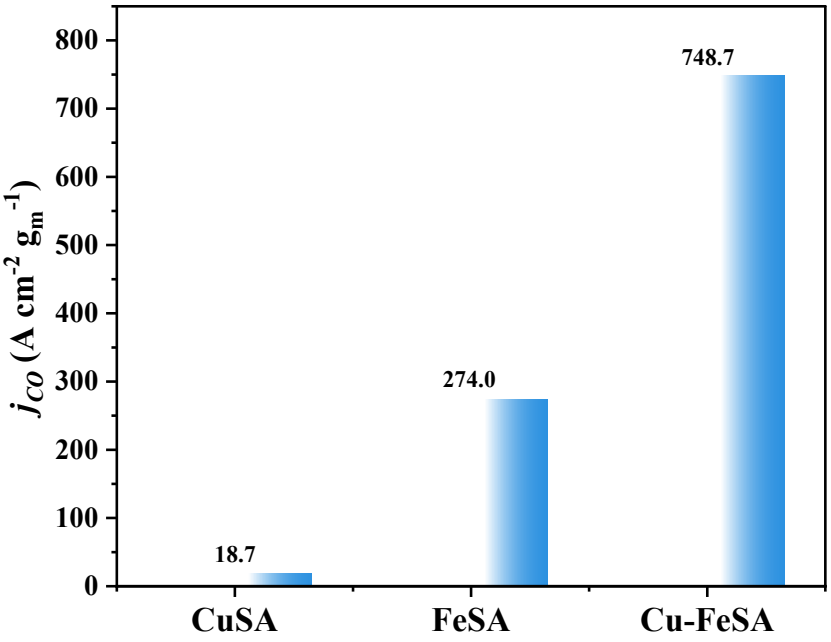

Figure S17. Metal loading-normalized CO partial current densities for CuSA, FeSA and Cu-FeSA at −1.26 V (vs RHE).

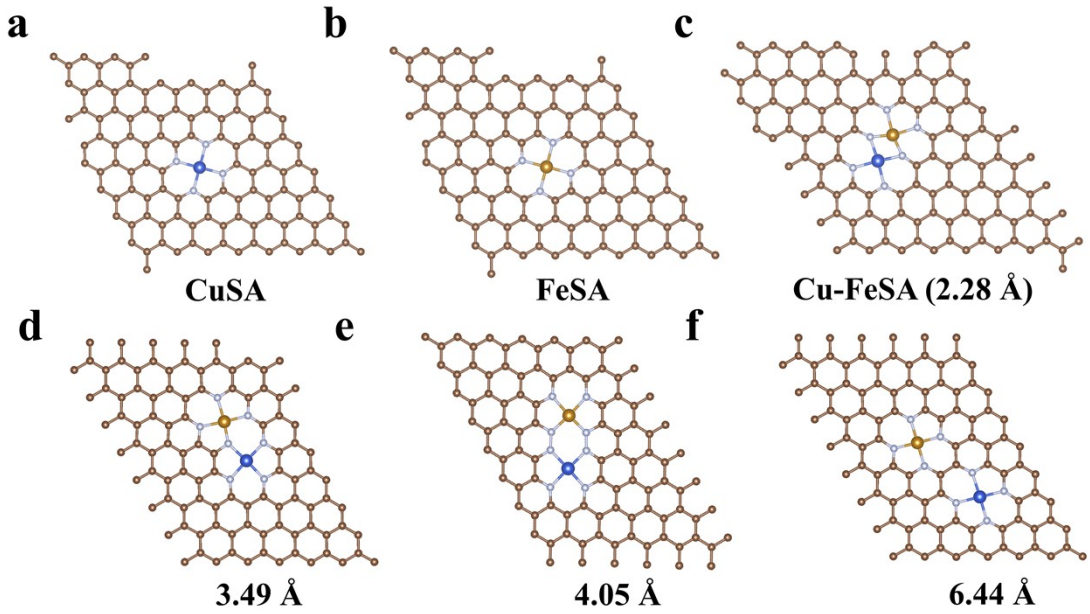

Figure R18. The models of Cu−N_4, Fe−N_4, Fe−Cu−N_4 and different Cu−Fe distances.

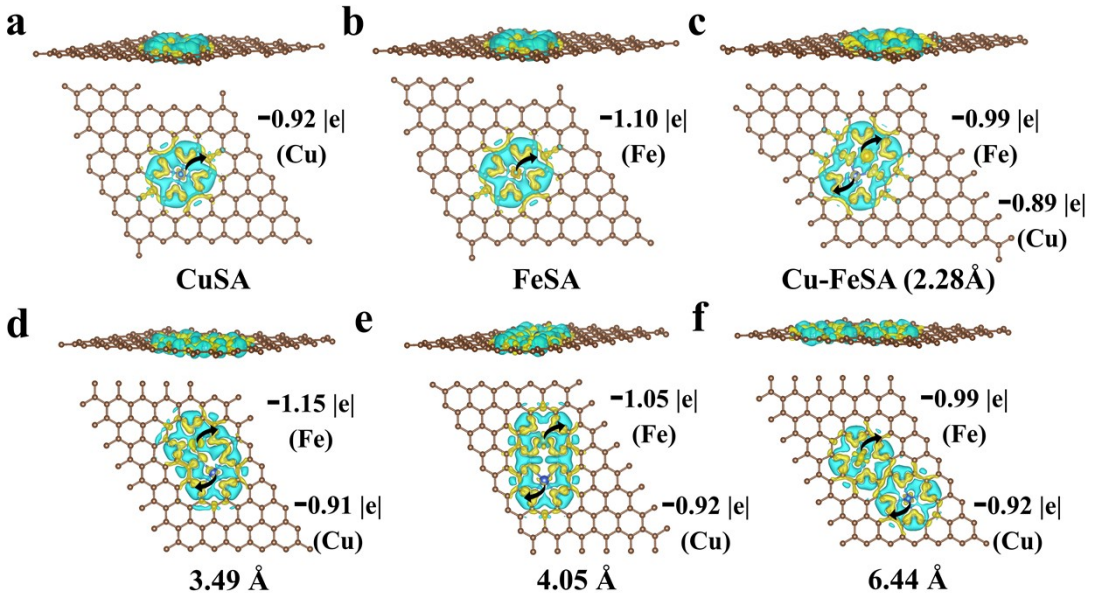

Figure S19. Bader charges analysis of Cu−N_4, Fe−N_4, Fe−Cu−N_4 and different Cu−Fe distances.

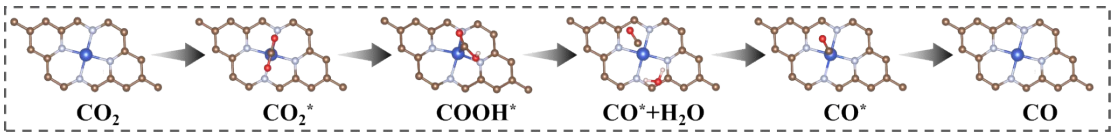

Figure S20. Optimized structures of all reaction intermediates involved in the CO_2-CO reduction pathway at Cu−N_4 site.

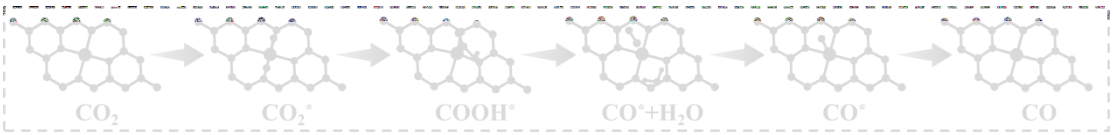

Figure S21. Optimized structures of all reaction intermediates involved in the CO_2-CO reduction pathway at Cu−N_4 site.

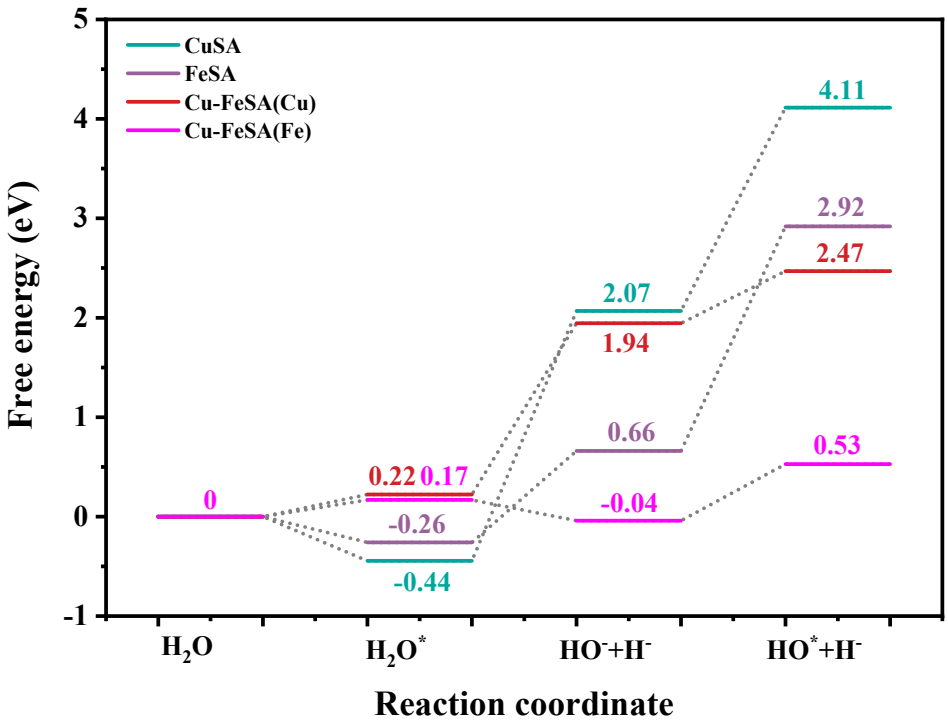

Figure S22. Free energy diagram for HER at Cu−N_4, Fe−N_4, Fe−Cu−N_4 (Cu) and Fe−Cu−N_4 (Fe) sites.

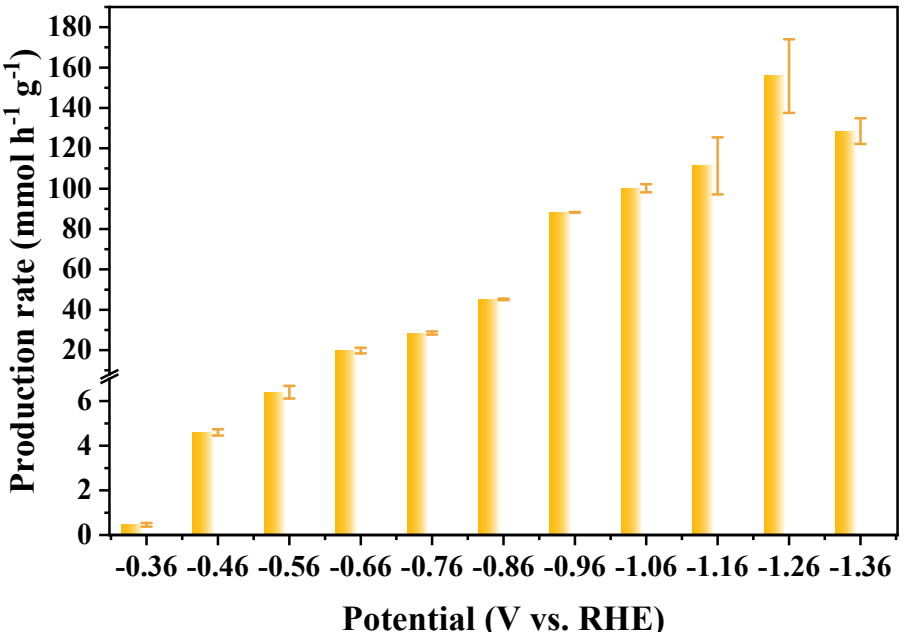

Figure S23. Production rate of CO_2-to-CO at H-cell reactor for Cu-FeSA.

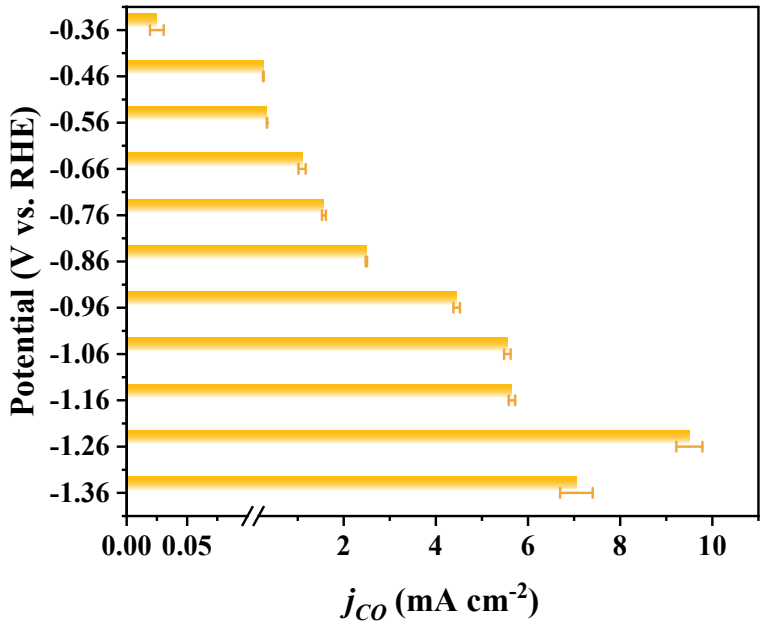

Figure S24. CO partial current density of Cu-FeSA.

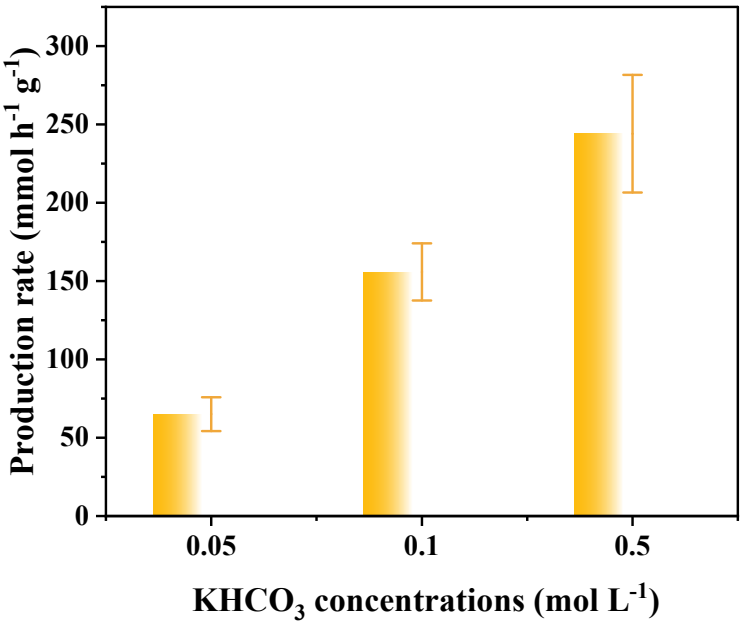

Figure S25. CO production rate under different electrolyte concentrations.

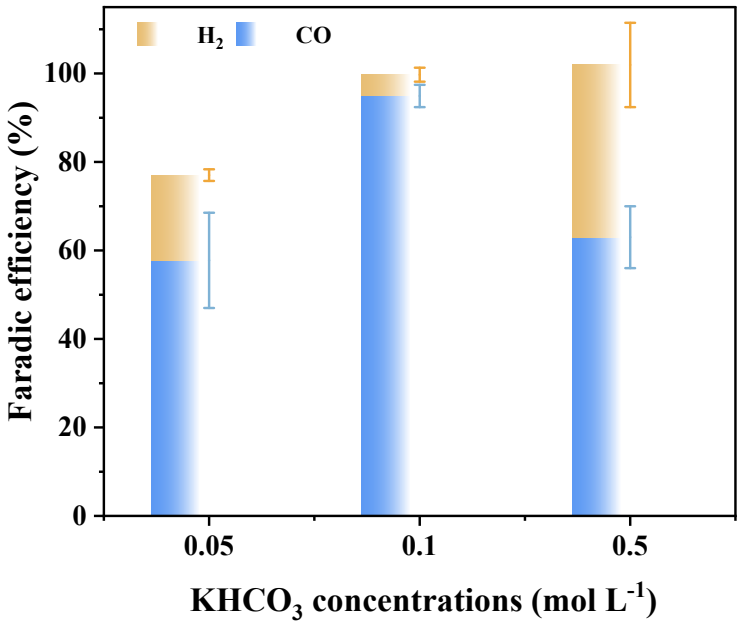

Figure S26. Faradic efficiency at −1.26 V (vs RHE) for different $KHCO_3$ concentrations of Cu-FeSA.

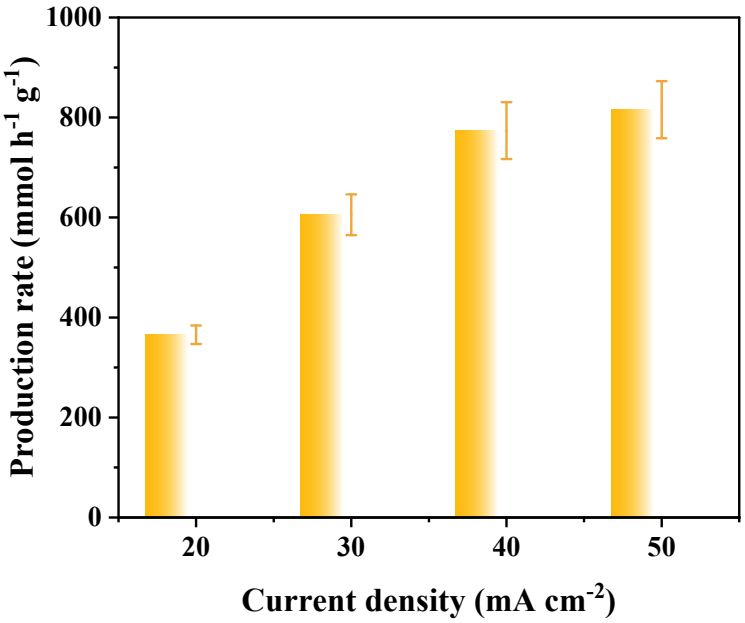

Figure S27. CO Production of Cu-FeSA at different current densities.

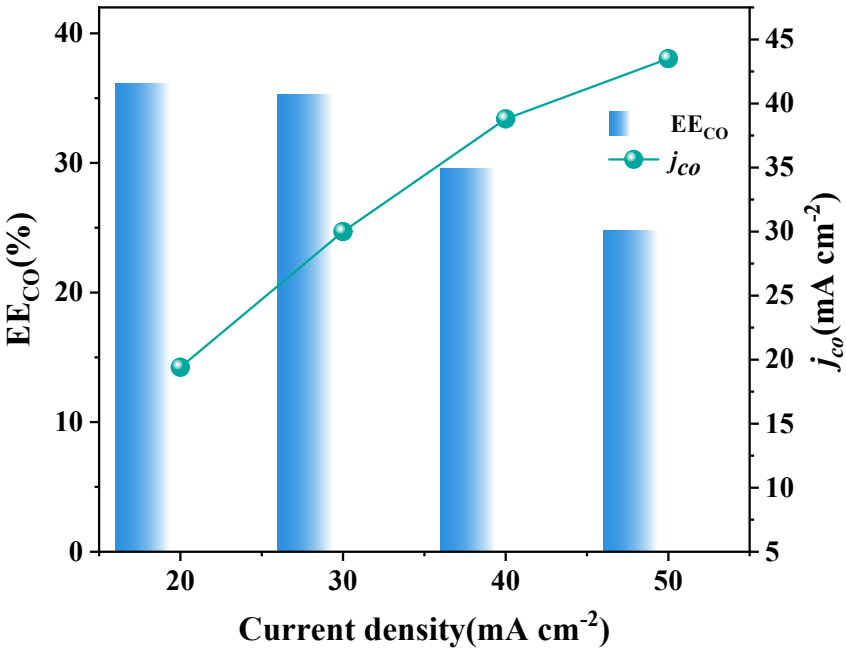

Figure S28. Full-cell energy efficiency and partial current density toward CO of Cu-FeSA in the flow cell.

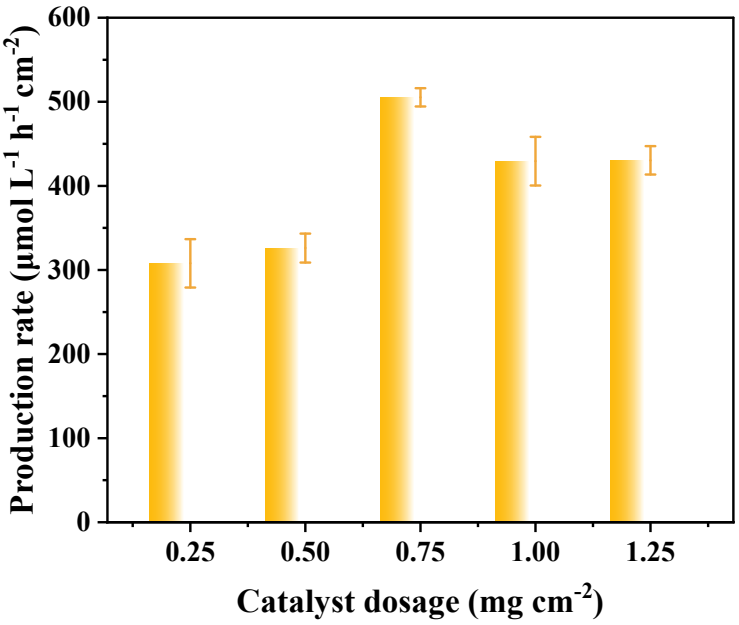

Figure S29. Production rate of CO_2-to-CO on Cu-FeSA in the flow-cell reactor.

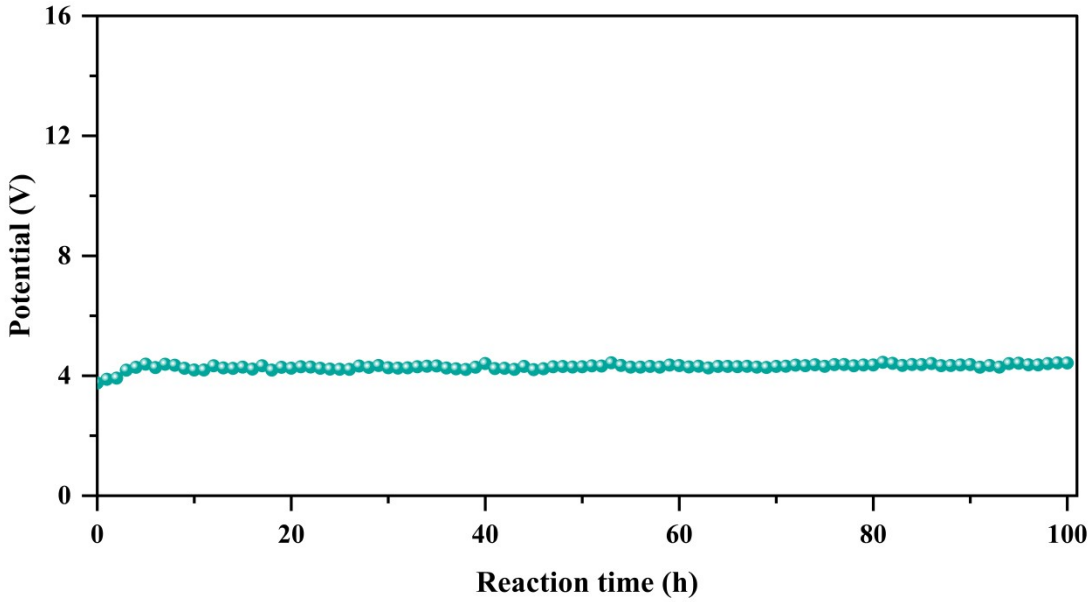

Figures S30. 100 h long time voltage stability test.

Supplementary Tables

Table S1. Quantification of Cu and Fe species in the as prepared electrocatalysts by ICP-OES.

Samples	Cu-FeSA	CuSA	FeSA
Content of Cu (wt.%)	0.856	0.848	/
Content of Fe (wt.%)	0.149	/	0.925

Table S2. The atomic content of each element in the prepared electrocatalysts was quantified using XPS.

Catalysts	Cu-FeSA	CuSA	FeSA
Atomic of C (%)	85.93	84.23	88.24
Atomic of N (%)	5.06	9.55	1.88
Atomic of O (%)	8.28	5.92	7.62
Atomic of Cu (%)	0.3	0.31	/
Atomic of Fe (%)	0.43	/	2.25

Table S3. EXAFS data fitting results of Samples (Cu).

Sample	Path	*CN*[a]	*R*(Å)[b]	σ^2 (Å^2)[c]	ΔE_0(eV)[d]	*R* factor
Cu K-edge (S_0^2=0.7469)						
Cu foil	Cu-Cu	12.0*	2.54	0.007	4.2±0.4	0.008
Cu-FeSA	Cu-N	4.1±0.2	1.97	0.005	-4.8±0.5	0.005

[a]*CN*, coordination number; [b]*R*, the distance to the neighboring atom; [c]σ^2, the Mean Square Relative Displacement (MSRD); [d]ΔE_0, inner potential correction; R factor indicates the goodness of the fit. S_0^2 was fixed to 0.7469, according to the experimental EXAFS fit of the sample foil by fixing CN as the known crystallographic value. This value was fixed during EXAFS fitting, based on the known structure of Cu foil. Data ranges $3.0 \leq k \leq 11.0$ Å^{-1}, $1.0 \leq R \leq 3.0$ Å. The Debye-Waller factors and ΔRs are based on the guessing parameters and constrained for paths.

Table S4. EXAFS data fitting results of Samples (Fe).

Sample	Path	*CN*[a]	*R*(Å)[b]	σ^2 (Å^2)[c]	ΔE_0(eV)[d]	*R* factor
Fe K-edge (S_0^2=1.0974)						
Fe foil	Fe-Fe	8	2.47	0.008	5.2±0.5	0.012
	Fe-Fe2	6	2.83	0.007		
Cu-FeSA	Fe-N	4.2±0.2	2.02	0.008	-3.0±0.4	0.005

[a]*CN*, coordination number; [b]*R*, the distance to the neighboring atom; [c]σ^2, the Mean Square Relative Displacement (MSRD); [d]ΔE_0, inner potential correction; R factor indicates the goodness of the fit. S_0^2 was fixed to 1.0974, according to the experimental EXAFS fit of the sample foil by fixing CN as the known crystallographic value. This value was fixed during EXAFS fitting, based on the known structure of Fe foil. Data ranges $3.0 \leq k \leq 10.0$ Å^{-1}, $1.0 \leq R \leq 3.0$ Å. The Debye-Waller factors and ΔRs are based on the guessing parameters and constrained for paths.

Table S5. Metal leaching concentrations of the Cu-FeSA catalyst after stability testing by ICP-OES.

Cycle Number	Cu Leaching (mg L^{-1})	Fe Leaching (mg L^{-1})
1	0.155	0.149
5	0.006	0.039

Table S6. Comparison of Two-Electron CO_2 Reduction to CO in H-cell under alkaline conditions with currently reported work

Catalysts	Electrolyte	FE (%)	Potential (V vs. RHE)	Ref.
CNS-NiSA	0.5 M $KHCO_3$	95	-0.8	5
NiSA-NGA-900	0.5 M $KHCO_3$	90.2	-0.8	6
Ni-SNC	0.5 M $KHCO_3$	95	-0.8	7
Ni_1-N-C (Cl)	0.5 M $KHCO_3$	94.7	-0.7	8
NiSA-N-CNTs	0.5 M $KHCO_3$	91.3	-0.7	9
NC-CNTs (Ni)	0.5 M $KHCO_3$	90	-1.0	10
Ni-SAs@FNC	0.5 M $KHCO_3$	95	-0.77	11
V-$CuInSe_2$	0.5 M $KHCO_3$	91	-0.7	12
Chitin-2.5Fe	1 M $KHCO_3$	~90	-0.59	13
Co_1Cu_3@C	0.5 M $KHCO_3$	34	-0.7	14
Cd-MgAl-LDHs@RGO	0.1 M $KHCO_3$	91.5	-1.1	15
ZnO-UR	0.5 M $KHCO_3$	88	-0.95	16
Fe_3Ni_7-NC	0.5 M $KHCO_3$	81.3	-0.9	17
ZnO (1 0 1)	0.1 M $KHCO_3$	91.4	-0.9	18
ZnO-V_O-S	0.5 M $KHCO_3$	90	-1.1	19
CeNCl-CeO_2/Ni/N-C	0.5 M $KHCO_3$	90	-0.8	20
ZnO-NN	0.5 M $KHCO_3$	91.3	-0.88	21
$NiCd_{650}F_{0.2}$	0.1 M $KHCO_3$	90.3	-1.0	22
Cu-FeSA	0.1 M $KHCO_3$	95	-1.3	This work

Table S7. Comparison of Two-Electron CO_2 Reduction to CO in flow-cell under alkaline conditions with currently reported work

Catalysts	Electrolyte	FE (%)	*J* (mA cm^{-2})	Stability (h)	Ref.
Au/CeO_2/MWCNT	1 M KOH	51.87	200	20	23
ZrO_2@Ni-NC	1 M $KHCO_3$	96.8	200	12	24
Ni-NC	1 M $KHCO_3$	84.1	150	/	24
NiPc–OMe MDE	1 M $KHCO_3$	~99.5	300	40	25
CoPc@GO	1 M KOH	96.33	500	35	26
CoPc/GO	1 M KOH	74.5	500	/	26
FeZnNC	1 M KOH	~97	50-300	/	27
Co^{II}QPyPhen	1 M $KHCO_3$	~99	100	8	28
Ni@C_3N_4-CN	1 M $KHCO_3$	90	300	20	29
CoF_4Pc/CNT 2:30	0.5 M $KHCO_3$	91.8	29	2	30
Cu-FeSA	1 M $KHCO_3$	97	20	10	This work
		100	30		
		97	40		
		87	50		

References

(1) Kresse, G.; Furthmüller, J. Efficiency of Ab-Initio Total Energy Calculations for Metals and Semiconductors Using a Plane-Wave Basis Set. *Comput. Mater. Sci.* **1996**, *6* (1), 15–50.

(2) Kresse, G.; Furthmüller, J. Efficient Iterative Schemes for Ab Initio Total-Energy Calculations Using a Plane-Wave Basis Set. *Phys Rev B* **1996**, *54* (16), 11169–11186.

(3) Perdew, J. P.; Burke, K.; Ernzerhof, M. Generalized Gradient Approximation Made Simple. *Phys. Rev. Lett.* **1996**, *77* (18), 3865–3868.

(4) Kresse, G.; Joubert, D. From Ultrasoft Pseudopotentials to the Projector Augmented-Wave Method. *Phys Rev B* **1999**, *59* (3), 1758–1775.

(5) Zhao, X.; Huang, S.; Chen, Z.; Lu, C.; Han, S.; Ke, C.; Zhu, J.; Zhang, J.; Tranca, D.; Zhuang, X. Carbon Nanosheets Supporting Ni–N_3S Single-Atom Sites for Efficient Electrocatalytic CO_2 Reduction. *Carbon* **2021**, *178*, 488–496.

(6) Mou, K.; Chen, Z.; Zhang, X.; Jiao, M.; Zhang, X.; Ge, X.; Zhang, W.; Liu, L. Highly Efficient Electroreduction of CO_2 on Nickel Single-Atom Catalysts: Atom Trapping and Nitrogen Anchoring. *Small* **2019**, *15* (49), 1903668.

(7) Yang, X.; Cheng, J.; Lv, H.; Yang, X.; Ding, L.; Xu, Y.; Zhang, K.; Sun, W.; Zhou, J. Sulfur-Doped Unsaturated Ni-N3 Coordination for Efficient Electroreduction of CO_2. *Chem. Eng. J.* **2022**, *450*, 137950.

(8) Peng, J.-X.; Yang, W.; Jia, Z.; Jiao, L.; Jiang, H.-L. Axial Coordination Regulation of MOF-Based Single-Atom Ni Catalysts by Halogen Atoms for Enhanced CO_2 Electroreduction. *Nano Res.* **2022**, *15* (12), 10063–10069.

(9) Cheng, Y.; Zhao, S.; Johannessen, B.; Veder, J.; Saunders, M.; Rowles, M. R.; Cheng, M.; Liu, C.; Chisholm, M. F.; De Marco, R.; Cheng, H.; Yang, S.; Jiang, S. P. Atomically Dispersed Transition Metals on Carbon Nanotubes with Ultrahigh Loading for Selective Electrochemical Carbon Dioxide Reduction. *Adv. Mater.* **2018**, *30* (13), 1706287.

(10) Fan, Q.; Hou, P.; Choi, C.; Wu, T.; Hong, S.; Li, F.; Soo, Y.; Kang, P.; Jung, Y.; Sun, Z. Activation of Ni Particles into Single Ni–N Atoms for Efficient Electrochemical Reduction of CO_2. *Adv. Energy Mater.* **2020**, *10* (5), 1903068.

(11) Han, S.-G.; Ma, D.-D.; Zhou, S.-H.; Zhang, K.; Wei, W.-B.; Du, Y.; Wu, X.-T.; Xu, Q.; Zou, R.; Zhu, Q.-L. Fluorine-Tuned Single-Atom Catalysts with Dense Surface Ni-N_4 Sites on Ultrathin Carbon Nanosheets for Efficient CO_2 Electroreduction. *Appl. Catal. B Environ.* **2021**, *283*, 119591.

(12) Wang, J.; Zheng, X.; Wang, G.; Cao, Y.; Ding, W.; Zhang, J.; Wu, H.; Ding, J.; Hu, H.; Han, X.; Ma, T.; Deng, Y.; Hu, W. Defective Bimetallic Selenides for Selective CO_2 Electroreduction to CO. *Adv. Mater.* **2022**, *34* (3), 2106354.

(13) Sun, P.; Wang, X.; Zhu, M.; Ahmad, N.; Zhang, K.; Xu, X. Nitrogen Self-Doped Metal Free Catalysts Derived from Chitin via One Step Method for Efficient Electrocatalytic CO_2 Reduction to CO. *Catalysts* **2023**, *13* (5), 904.

(14) Song, C.; Wang, X.; Song, G.; Shi, G.; Wang, Y.; Yu, J.; Xie, X.; Sun, J. Electrocatalytic Reduction of CO_2 by Co-Cu Metastable Alloy Nanoparticles Derived from MOFs. *J. Alloys Compd.* **2024**, *994*, 174693.

(15) Ma, X.; Liu, T.; Liu, E.; Zhang, Y. Preparation and Performance of Cd-MgAl-LDHs@RGO in High Efficiency Electrocatalytic Reduction of CO_2 to CO. *Mol. Catal.* **2023**, *535*, 112876.
(16) Wang, H.; Xiao, Y.; Qi, Y.; Zhang, A.; Du, J.; Li, J.; Guo, T. Fabrication of ZnO Nanosheets Self-Assembled by Nanoparticles for Accelerated Electrocatalytic Reduction of CO_2 to CO. *Fuel* **2023**, *333*, 126431.
(17) Han, X.; Chang, Y.; Yue, T.; Jia, M.; Jia, J. Fe-Ni Bimetallic Composite N-Doped Carbon Catalyst for Electrocatalytic Reduction of CO_2 to Produce Efficient and Controlled Syngas. *J. Alloys Compd.* **2024**, *971*, 172772.
(18) Wang, J.; Zhu, Z.; Lin, Y.; Qi, X.; Li, Z.; Jiang, J.; Niu, X.; Chen, J. S.; Wu, R. Modulating Surface Zinc Species via Facet Engineering for Efficient Electroreduction of CO_2 to CO. *Chem. Eng. J.* **2024**, *481*, 148730.
(19) Wang, Y.; Kang, Y.; Miao, Y.; Jia, M.; Long, S.; Diao, L.; Zhang, L.; Li, D.; Wu, G. S-Dopant and O-Vacancy of Mesoporous ZnO Nanosheets Induce High Efficiency and Selectivity of Electrocatalytic CO_2 Reduction to CO. *Compos. Commun.* **2024**, *48*, 101890.
(20) Liu, L.; Wang, F.; Chu, X.; Zhang, L.; Zhang, S.; Wang, X.; Che, G.; Song, S.; Zhang, H. CeNCl-CeO_2 Heterojunction-Modified Ni Catalysts for Efficient Electroreduction of CO_2 to CO. *Adv. Energy Mater.* **2024**, *14* (2), 2301575.
(21) Umar, M.; Aljezan, M. Y.; Abdulazeez, I.; Amao, A. O.; Ganiyu, S. A.; Alhooshani, K. Modulating the Electrocatalytic Reduction of CO_2 to CO via Surface Reconstruction of ZnO Nanoshapes. *J. Sci. Adv. Mater. Devices* **2024**, *9* (3), 100748.
(22) Lu, B.; Liu, T.; Li, J. Porous Nickel-Based Catalyst Doped with Fluorine Can Efficiently Electrocatalyze the Reduction of CO_2 to CO. *J. Alloys Compd.* **2024**, *1008*, 176771.
(23) Kim, Y.; Kim, B.; Choi, H.; Kim, S.; Yun, Y.; Oh, J. Modulating the Electronic Structure of Au Using a Heterostructure for Efficient Electrochemical CO_2 Reduction. *Chem. Eng. J.* **2023**, *461*, 142126.
(24) Wang, X.; Feng, S.; Lu, W.; Zhao, Y.; Zheng, S.; Zheng, W.; Sang, X.; Zheng, L.; Xie, Y.; Li, Z.; Yang, B.; Lei, L.; Wang, S.; Hou, Y. A New Strategy for Accelerating Dynamic Proton Transfer of Electrochemical CO_2 Reduction at High Current Densities. *Adv. Funct. Mater.* **2021**, *31* (50), 2104243.
(25) Zhang, X.; Wang, Y.; Gu, M.; Wang, M.; Zhang, Z.; Pan, W.; Jiang, Z.; Zheng, H.; Lucero, M.; Wang, H.; Sterbinsky, G. E.; Ma, Q.; Wang, Y.-G.; Feng, Z.; Li, J.; Dai, H.; Liang, Y. Molecular Engineering of Dispersed Nickel Phthalocyanines on Carbon Nanotubes for Selective CO_2 Reduction. *Nat. Energy* **2020**, *5* (9), 684–692.
(26) Lv, X.; Liu, Q.; Yang, H.; Wang, J.; Wu, X.; Li, X.; Qi, Z.; Yan, J.; Wu, A.; Cheng, T.; Wu, H. B. Nanoconfined Molecular Catalysts in Integrated Gas Diffusion Electrodes for High-Current-Density CO_2 Electroreduction. *Adv. Funct. Mater.* **2023**, *33* (32), 2301334.
(27) Tang, Q.; Hao, Q.; Zhu, Q.; Wu, J.; Huang, K.; Liu, K.; Lu, J. Intrinsic Electron Transfer in Heteronuclear Dual-Atom Sites Facilitates Selective Electrocatalytic Carbon Dioxide Reduction. *Adv. Energy Mater.* **2025**, *15* (7), 2403778.

(28) Sun, L.; Reddu, V.; Xi, S.; Dai, C.; Sheng, Y.; Su, T.; Fisher, A. C.; Wang, X. Cobalt Quaterpyridine Complexes for Highly Efficient Heterogeneous CO_2 Reduction in Aqueous Media. *Adv. Energy Mater.* **2022**, *12* (34), 2202108.
(29) Wang, Q.; Liu, K.; Hu, K.; Cai, C.; Li, H.; Li, H.; Herran, M.; Lu, Y.-R.; Chan, T.-S.; Ma, C.; Fu, J.; Zhang, S.; Liang, Y.; Cortés, E.; Liu, M. Attenuating Metal-Substrate Conjugation in Atomically Dispersed Nickel Catalysts for Electroreduction of CO_2 to CO. *Nat. Commun.* **2022**, *13* (1), 6082.
(30) Li, M.; Xu, J.; Qi, F.; Wang, Y.; Yan, C.; Xu, J. Facile Preparation of Tetrafluoro-Substituted Cobalt Phthalocyanine Nanorods Attached on Carbon Nanotubes for Efficient Electrocatalytic CO_2 Reduction. *J. Solid State Electrochem.* **2023**, *27* (5), 1269–1278.